

This is a self-archived version of an original article. This version may differ from the original in pagination and typographic details.

Author(s): López-Estrada, Omar; Selenius, Elli; Zuniga-Gutierrez, Bernardo; Malola, Sami; Häkkinen, Hannu

Title: Cubic aromaticity in ligand-stabilized doped Au superatoms

Year: 2021

Version: Accepted version (Final draft)

Copyright: © 2021 Author(s)

Rights: In Copyright

Rights url: <http://rightsstatements.org/page/InC/1.0/?language=en>

Please cite the original version:

López-Estrada, O., Selenius, E., Zuniga-Gutierrez, B., Malola, S., & Häkkinen, H. (2021). Cubic aromaticity in ligand-stabilized doped Au superatoms. *Journal of Chemical Physics*, 154(20), Article 204303. <https://doi.org/10.1063/5.0050127>

Cubic aromaticity in ligand-stabilized doped Au superatoms

Cite as: J. Chem. Phys. **154**, 204303 (2021); <https://doi.org/10.1063/5.0050127>

Submitted: 12 March 2021 . Accepted: 07 May 2021 . Published Online: 25 May 2021

 Omar López-Estrada,  Elli Selenius,  Bernardo Zuniga-Gutierrez, Sami Malola, and  Hannu Häkkinen

COLLECTIONS

Paper published as part of the special topic on [From Atom-Precise Nanoclusters to Superatom Materials](#)



View Online



Export Citation



CrossMark

ARTICLES YOU MAY BE INTERESTED IN

[More than little fragments of matter: Electronic and molecular structures of clusters](#)

The Journal of Chemical Physics **154**, 200901 (2021); <https://doi.org/10.1063/5.0054222>

[Gas-phase studies of chemically synthesized Au and Ag clusters](#)

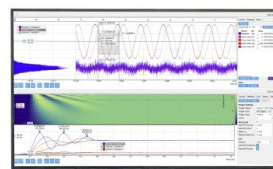
The Journal of Chemical Physics **154**, 140901 (2021); <https://doi.org/10.1063/5.0041812>

[A joint experimental and theoretical study on structural, electronic, and magnetic properties of \$\text{MnGe}_n^-\$ \(\$n = 3-14\$ \) clusters](#)

The Journal of Chemical Physics **154**, 204302 (2021); <https://doi.org/10.1063/5.0053414>

Challenge us.

What are your needs for
periodic signal detection?



Zurich
Instruments

Cubic aromaticity in ligand-stabilized doped Au superatoms

Cite as: J. Chem. Phys. 154, 204303 (2021); doi: 10.1063/5.0050127

Submitted: 12 March 2021 • Accepted: 7 May 2021 •

Published Online: 25 May 2021



View Online



Export Citation



CrossMark

Omar López-Estrada,¹ Elli Selenius,¹ Bernardo Zuniga-Cutierrez,² Sami Malola,¹
and Hannu Häkkinen^{1,3,a)}

AFFILIATIONS

¹ Department of Physics, Nanoscience Center, University of Jyväskylä, FI-40014 Jyväskylä, Finland

² Departamento de Química, Universidad de Guadalajara, CUCEI, Blvd. Marcelino García Barragán 1421, C. P. 44430 Guadalajara, Jalisco, Mexico

³ Department of Chemistry, Nanoscience Center, University of Jyväskylä, FI-40014 Jyväskylä, Finland

Note: This paper is part of the JCP Special Topic on From Atom-Precise Nanoclusters to Superatom Materials.

^{a)} Author to whom correspondence should be addressed: hannu.j.hakkinen@jyu.fi

ABSTRACT

The magnetic response of valence electrons in doped gold-based $[M@Au_8L_8]^q$ superatoms ($M = Pd, Pt, Ag, Au, Cd, Hg, Ir,$ and Rh ; $L = PPh_3$; and $q = 0, +1, +2$) is studied by calculating the gauge including magnetically induced currents (GIMIC) in the framework of the auxiliary density functional theory. The studied systems include 24 different combinations of the dopant, total cluster charge, and cluster structure (cubic-like or oblate). The magnetically induced currents (both diatropic and paratropic) are shown to be sensitive to the atomic structure of clusters, the number of superatomic electrons, and the chemical nature of the dopant metal. Among the cubic-like structures, the strongest aromaticity is observed in Pd- and Pt-doped $[M@Au_8L_8]^0$ clusters. Interestingly, Pd- and Pt-doping increases the aromaticity as compared to a similar all-gold eight-electron system $[Au_8L_8]^{+1}$. With the recent implementation of the GIMIC in the deMon2k code, we investigated the aromaticity in the cubic and butterfly-like $M@Au_8$ core structures, doped with a single M atom from periods 5 and 6 of groups IX–XII. Surprisingly, the doping with Pd and Pt in the cubic structure increases the aromaticity compared to the pure Au case not only near the central atom but encompassing the whole metallic core, following the aromatic trend $Pd > Pt > Au$. These doped (Pd, Pt) $@Au_8$ nanoclusters show a closed shell $1S^21P^6$ superatom electronic structure corresponding to the cubic aromaticity rule $6n + 2$.

Published under an exclusive license by AIP Publishing. <https://doi.org/10.1063/5.0050127>

I. INTRODUCTION

The ubiquitous concept of aromaticity¹ has been popularized since the discovery of benzene by Faraday in 1825² and Kekulé's proposal for its structure in 1865.³ Even though aromaticity has been widely used to explain the stability in molecules and coordination compounds,^{4,5} related with spectroscopy⁶ and magnetic properties,⁷ and employed to describe chemical reactivity^{8,9} in several compounds, there is no consensus¹⁰ about its nature due to the lack of a quantum mechanical observable to directly measure it.

The high symmetry of organic molecules or compounds is commonly related to aromaticity, as is the stability of their electronic structure related to the closed-shell structure.^{11,12} Although there have been several efforts to establish a criterion to determine aromaticity in the different bare and protected metal clusters^{13–17} and

successful attempts have been made to indirectly correlate its effects with measurable quantities such as chemical shifts in nuclear magnetic resonance (NMR);¹⁸ e.g., the aromatic nature of a compound can be observed through the down-field shift in the ¹H probe NMR caused by magnetic shielding^{2,7}, there are still some questions to address. Indeed, the cubic geometry has been explored in different systems to find a remarkable stability by relating the electron delocalization and the electronic structure with a concept named cubic aromaticity. To mention some examples, there have been studies about this cubic aromaticity in Zn_8 ,¹⁹ Mn_8 ,²⁰ $Co_{13}O_8$,²¹ and CBe_8H_{12} ²² clusters.

Aromaticity has also been studied in doped monolayer-protected gold superatoms.²³ These systems are of interest because of the promising applications that can enhance targeted physico-chemical properties, such as luminescence and catalysis,^{24,25} by the

rational design and tuning of the metallic core and tailoring of the surface ligand–core interface.^{26–28}

Consequently, the effects of the closed shell electronic structure and the composition of the metallic core on the physico-chemical properties have been explored. For example, the doping effect for $M@Au_{24}(SR)_{18}$ superatoms has been previously investigated for dopants such as Pd, Pt, Cd, and Hg.^{29–31} The preferred sites were observed to be at the center location for Pd and Pt and on the surface of the core for Cd and Hg.³² The doping effect has also been studied for the elements of the group IX, Rh, and Ir.³³ Similarly, as for Pd and Pt, the endohedral location was preferred for the dopants in $M@Au_{24}(SR)_{18}^{(-1,-3)}$ clusters.

The hydrogen evolution reaction was studied in doped $M@Au_{24}$ nanoclusters where $M = Pd$ and Pt .³⁴ Doping was found to decrease the adsorption free energy for hydrogen, thus improving the catalytic activity of the doped clusters, with Pt doped clusters having the best performance.

An additional example of a widely studied system are the superatoms with a metal core based on Au_9 . Of these compositions, clusters without doping protected by PPh_3 have been crystallized in three different symmetries: butterfly-like with D_{2h} symmetry,³⁵ crown-like with approximately D_{4d} symmetry,^{36,37} and metastable cubic with O_h symmetry recently obtained by the crystallization of a metastable state.³⁸ As a consequence of the interest in tuning the composition of the Au metal cores, clusters $M@Au_8$ with Pd³⁹ or Pt⁴⁰ at the center have also been experimentally observed. These clusters can be used in the synthesis of larger nanoclusters via hydride doping⁴¹ and have possible applications in catalysis,⁴² motivating studies of their formation⁴³ and further modification.⁴⁴

In this work, we have systematically studied the magnetic response of valence electrons of 24 different doped gold-based $[M@Au_8L_8]^q$ superatoms ($M = Pd, Pt, Ag, Au, Cd, Hg, Ir,$ and Rh ; $L = PPh_3$; and $q = 0, +1, +2$) having 6–10 delocalized superatom electrons in the metal core, with the aim of using the magnetically induced diatropic current as the descriptor for aromaticity.⁴⁵ We have employed our recent implementation of the gauge-including magnetically induced currents (GIMIC)⁴⁶ in the framework of the auxiliary density functional theory (ADFT). The implementation uses the gauge-independent atomic orbitals (GIAO) introduced by London⁴⁷ to solve the gauge origin problem in the computation of the magnetic properties of molecules and takes advantage of efficient recurrence relations to compute the shielding tensor,⁴⁸ resulting in a high performance of the computation of the magnetically induced current susceptibility. We show that the magnetically induced current is sensitive to the atomic structure of the clusters, the number of superatomic electrons, and the chemical nature of the dopant metal.

II. THEORY AND METHODS

A. Response of electrons to an external magnetic field

When a diamagnetic object (molecule and nanocluster) is under the influence of an external magnetic field \vec{B} , the movement of the electrons generates an induced current that is a sum of diamagnetic and paramagnetic contributions. The induced current can flow in two directions relative to the external magnetic field:

a classical diatropic one (clockwise) and a nonclassical paratropic one (anticlockwise). Molecules or nanostructures that experience a strong diatropic response are called aromatic, those that sustain mainly paratropic currents are called antiaromatic, and those that have almost the same strengths for both contributions are called non-aromatic.⁴⁹

Thus, a formally called magnetic aromaticity/antiaromaticity must be related to the ability of a ring or arrangements of atoms in a closed chain to sustain a global induced current (clockwise/counterclockwise direction) in the presence of an external perpendicular magnetic field. This induced global current circulation is commonly known as the ring-current model.^{50,51}

Density functional theory (DFT) computations have been used to indicate the molecular response properties under the influence of an external magnetic field (e.g., on the magnetic susceptibilities⁵² and chemical shifts⁴⁸). In fact, these properties are computed as second order energy change ($\Delta E^{(2)}$) in a molecule/nanoparticle interacting with the external magnetic field. Thus, the magnetic shielding tensor $\sigma_{C,\eta\lambda}$ ($\eta, \lambda = x, y, z$) at the position of the nucleus C can be computed as the second derivative of the energy with respect to the external magnetic field \vec{B} and the nuclear magnetic moment $\vec{\mu}_C$ in the limit $\vec{B}, \vec{\mu}_C \rightarrow 0$,⁵³

$$\sigma_{C,\eta\lambda} = \frac{\partial^2 E}{\partial B_\lambda \partial \mu_{C,\eta}}. \quad (1)$$

Another second order energy expression involves a divergenceless vector potential $\vec{A}(\vec{r})$ ($\nabla \cdot \vec{A}(\vec{r}) = 0$),

$$\Delta E^{(2)} = - \sum_{C=1}^{Nuclei} \int \vec{A}_C(\vec{r}) \cdot \vec{J}(\vec{r}) d\vec{r}, \quad (2)$$

where $\vec{J}(\vec{r})$ is the electron current density. Then, substituting the explicit form of the vector potential⁴⁶ and differentiating with respect to the Cartesian components of the vectors $\vec{\mu}_C$ and \vec{B} , we get the nuclear magnetic shielding tensor via the Biot–Savart law,^{50,54–60}

$$\sigma_{C,\eta\lambda} = - \frac{\mu_0}{4\pi} \sum_{\alpha,\tau=x}^z \varepsilon_{\eta\alpha\tau} \int \frac{\alpha - C_\alpha}{|\vec{r} - \vec{C}|^3} \mathcal{J}_\tau^{(\lambda)}(\vec{r}) d\vec{r}, \quad (3)$$

where $\varepsilon_{\eta\alpha\tau}$ ($\eta, \alpha, \tau = x, y, z$) is the Levi-Civita tensor and \vec{C} is the position of the nucleus C (within the implementation, we employ a.u., and then, $\mu_0/4\pi = 1/c^2$). The quantity $\mathcal{J}_\tau^{(\lambda)}$ is defined as

$$\mathcal{J}_\tau^{(\lambda)} \equiv \frac{\partial \mathcal{J}_\tau}{\partial B_\lambda}. \quad (4)$$

It is an element of the so-called current density tensor (CDT),^{59,61,62} which characterizes the response of the current density to an external magnetic field. λ indicates differentiation with respect to the corresponding Cartesian coordinate of the magnetic field.

Finally, the magnetically induced current (MIC) density can be calculated as the first order correction to the total current density. The MIC only includes direct dependence on basis functions, first derivatives of basis functions, and density matrix and magnetically perturbed density matrix. In this work, those quantities are computed in a standard SCF procedure in deMon2k.⁶³

B. Computational details

Ground state DFT calculations were performed starting from crystallographic data (cube³⁸ and butterfly³⁵) using the real-space grid based GPAW program.^{64,65} The frozen core approximation was used for all the elements, with 15 valence electrons for Rh and Ir, 16 for Pd and Pt, 17 for Ag, 11 for Au, 12 for Cd, and 18 for Hg. The projector augmented wave (PAW) setups for heavy metals included scalar-relativistic corrections. The structures were optimized employing the generalized gradient approximation (PBE) exchange-correlation functional.⁶⁶ The optimization was finished when the residual forces on each atom were less than 0.05 eV/Å. The real-space grid spacing was 0.2 Å. To identify the symmetries of the superatomic orbitals, the Y_{lm} analysis⁶⁷ was performed for each cluster around the center of mass with a cut-off radius of 4.0 Å.

The magnetically induced current density was computed by the recent implementation⁴⁶ in deMon2k⁶³ employing gauge-including magnetically induced currents theory. The Stuttgart–Dresden (SDD) pseudopotential⁶⁸ (Rh and Ir—17 valence electrons, Pd and Pt—18 valence electrons, Ag and Au—19 valence electrons, and Hg and Cd—20 valence electrons) along with the DZVP⁶⁹ basis set (H, C, and P). PBE⁶⁶ was used to consider the exchange and correlation effects. All the computations were performed in combination with the GEN-A2* auxiliary function set.

III. RESULTS AND DISCUSSION

The clusters studied in this work with composition $[M@Au_8(PPh_3)_8]^q$ ($q = 0, +2$: M = Cd, Pd, Pt, and Hg; and $q = +1$: M = Rh, Ag, Ir, and Au) were obtained by doping the corresponding all-gold clusters: the nearly perfect body centered cubic (BCC) structure³⁸ and the approximate D_{2h} symmetry derived from an icosahedron,³⁵ as depicted in Fig. 1. These structures were chosen for their close similarity. Considering only the metal core, the transformation from the cubic shape to the butterfly shape can be achieved by compressing the distances of the Au atoms located on the yz plane in the y -coordinate and elongating them in the z -coordinate. For the sake of simplicity, we employ a notation for the two different structures of clusters $[M@Au_8L_8]^{q=0,+1,+2}$ (L = PPh₃) as $M@1^{q=0,+1,+2}$ for the cubic structures and $M@2^{q=0,+1,+2}$ for the butterfly-like structures, as shown in Fig. 1. In both cases, the Au based structures were doped with the single atom (Rh, Ir,

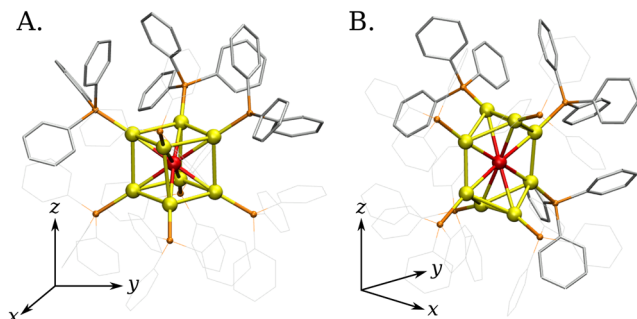


FIG. 1. (a) Cubic ($M@1^{q=0,+1,+2}$) and (b) butterfly-like ($M@2^{q=0,+1,+2}$) structures. The doping element is indicated by highlighting the central atom in red.

Pd, Pt, Ag, Cd, and Hg) occupying the central position. All the hypothetical systems were optimized, as discussed in Sec. II B. The total energies, energy differences, and HOMO–LUMO (H–L) gaps are summarized in Tables S1 and S2.

A. Geometrical description

The distances (r in Å) from the central atom to the eight surrounding Au atoms can be easily seen in Fig. 2. All the $M@1^q$ structures preserved an approximately cubic structure after the geometry optimization, where small distortions from the perfect BCC structure were observed. In the same way, all the $M@2^q$ butterfly-like structures preserved the D_{2h} symmetry, with the main differences with respect to the pure Au_9 core located in the longest distance from the central atom. To verify the different distortions with respect to the pure Au_9 cases, the principal moments of inertia were computed for all the structures $M@1^q$ and $M@2^q$, as summarized in Table S3, and the ratio with respect to the highest moment of inertia I_1 in Table S4. As shown in the bottom panel of Fig. 2, the shapes of the metallic core are not perfect cubes in any doping structure neither in the pure Au_9 case where the distances range from 2.68 to 2.70 Å (see Table S5). However, in any case, the structures were distorted, and they were still not far away from the BCC structure, as demonstrated by the ratio of the moments of inertia (Table S4). For the cubic structures, the shortest distances were observed for $Pd@1^0$ (2.64–2.66 Å) with $Hg@1^{+2}$ being the structure that has the most expanded structure (2.72–2.74 Å) (Table S5). In the case of the butterfly-like structures, two sets (4:4) of characteristic distances were shown (Table S5). The shortest ones were observed in $Rh@2^{+1}$ and the longest in $Hg@2^{+2}$.

B. Electronic structure

A criterion for the closed electronic structures is determined by the number of valence electrons (n) confined in the superatomic core given by the following equation first proposed by some of us:⁶⁷

$$n = \sum_{x=1}^N v_x - j - q, \quad (5)$$

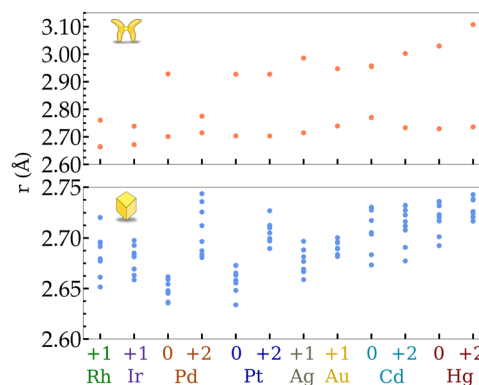


FIG. 2. Distances from the central atom to the surrounding eight Au atoms for the cubic (bottom row) $M@1^{q=0,+1,+2}$ and butterfly-like (top row) $M@2^{q=0,+1,+2}$ structures. The doping element and charge are indicated in different colors.

TABLE I. Closed electronic structure configuration for the lowest minimum energy of $M@(1, 2)^q$. Valence electrons provided by the dopant atom M (ν), total charge (q), and number of superatom electrons (n).

ν	q	n	M	$M@1^q$	$M@2^q$	M	$M@1^q$	$M@2^q$
-1	+1	6e	Ir	...	$1S^21P^4$	Rh	...	$1S^21P^4$
0	0	8e	Pd	$1S^21P^6$...	Pt	$1S^21P^6$...
0	+2	6e	Pd	...	$1S^21P^4$	Pt	...	$1S^21P^4$
1	+1	8e	Ag	...	$1S^21P_{y,z}^41D_{z^2}^2$	Au	$1S^21P^6$...
2	0	10e	Cd	...	$1S^21P_{y,z}^41D_{z^2}^21P_x^2$	Hg	...	$1S^21P_{y,z}^41D_{z^2}^21P_x^2$
2	+2	8e	Cd	...	$1S^21P_{y,z}^41D_{z^2}^2$	Hg	...	$1S^21P_{y,z}^41D_{z^2}^2$

where ν_x is the number of valence electrons provided by the x th constituent metal atom, N is the number of metal atoms, j is the number of one-electron-withdrawing ligands, and q is the total charge.

The number of valence electrons ν donated by the different dopant atoms and the superatomic electron count according to Eq. (5) can be seen in Table I. The superatomic electron configuration is also shown for the most stable isomer (1 or 2) of each cluster. These configurations were based on the Y_{lm} analysis,⁶⁷ which was performed for the clusters to distinguish the spherical symmetries of the frontier orbitals, as visualized in Figs. S1–S4. In the following, we discuss the electronic structures based on the chemical characterization (ν) from the dopant atom.

1. Ir/Rh @ Au₈

As shown in Table I, Ir and Rh have $\nu = -1$, making them electron-withdrawing dopants that diminish the superatomic electron count. Thus, the doped clusters with a charge of +1 are six-electron superatoms. Due to the splitting of the P orbitals, all these clusters have relatively large H–L gaps (0.89–1.14 eV). The (Ir, Rh)@2⁺¹ isomers have large H–L gaps and lower energies than their cubic counterparts. For the (Ir, Rh)@2⁺¹ clusters, HOMO and HOMO-1 are not superatomic orbitals, but localized d orbitals of the central dopant atom. LUMO in both, however, is the $1P_x$ orbital upshifted due to the Jahn–Teller effect. In the (Ir, Rh)@1⁺¹ isomers, the superatomic electron configuration is $1S^21P^4$. However, some of the frontier orbitals on the occupied side show d-type symmetry and have a strong contribution from the orbitals from the dopant.

2. Pd/Pt @ Au₈

Pd and Pt provide zero valence electrons to the superatom, making them neutral dopants. The (Pd,Pt)@1⁰ clusters are thus eight-electron superatoms, with the shell-closing $1S^21P^6$ and significant H–L gaps of 1.43 eV and 1.51 eV, respectively. In the (Pd, Pt)@2⁰ cluster, the HOMO and HOMO-1 are localized d orbitals of the central atom, as shown in Fig. S2. The H–L gap is reduced compared to the cubic isomers, which are also lower in energy.

In the (Pd, Pt)@2⁺² clusters with the $1S^21P^4$ superatomic electron configuration, the Jahn–Teller effect causes the 1P orbitals to split into three non-degenerate orbitals. The $1P_z$ orbital (see Fig. S2) is downshifted due to the elongation of the cluster in the z-direction (lowest moment of inertia I_3 ; see Table S3) and the $1P_x$ is upshifted (highest moment of inertia I_1 ; see Table S3). This results in the large H–L gap of these six-electron superatoms, as shown in Fig. 3(b). The

cubic isomers (Pd,Pt)@1⁺² experience somewhat smaller splitting due to the more symmetric shape of the metal core and consequently also have a smaller H–L gap. The cubic isomers are also less stable, as shown in Fig. 3(a).

3. Ag/Au @ Au₈

Au and Ag both have $\nu = +1$, making the doped clusters of $q = +1$ eight-electron superatoms. (Au, Ag)@1⁺¹ both have a configuration of $1S^21P^6$. For the Ag cluster, the three P orbitals are almost degenerate, whereas for Au, $1P_z$ is a little higher in energy, reflecting the slightly larger distribution in the principle moments of inertia, as shown in Table S4. The electronic structure of (Au, Ag)@2⁺¹ can be written as $1S^21P_{y,z}^41D_{z^2}^2$. Here again, the $1P_x$ orbital is significantly upshifted and also the $1D_{z^2}$ orbital downshifted due to the shape of the metal core, causing the change in the filling order of the superatomic orbitals. As a consequence, the H–L gap remains large,

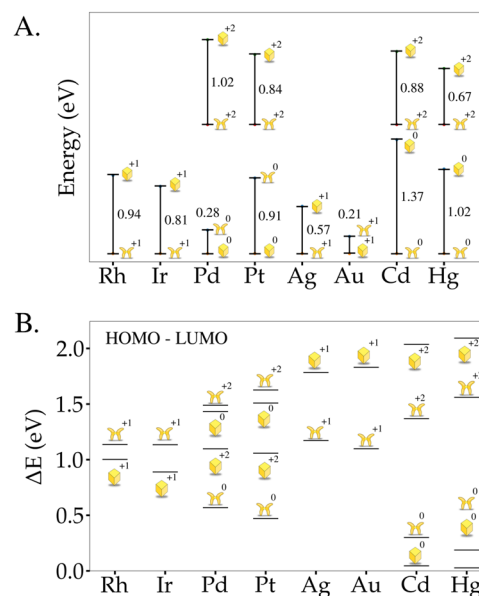


FIG. 3. (a) The relative energies for the two isomers for all the different dopings and charge states. The numbers and the lengths of the vertical bars indicate the difference in energy between the isomers. The vertical position of the bars has no physical meaning. (b) The HOMO–LUMO gaps for the same systems.

although smaller than that for the cubic isomers. The lower-energy isomer is **1** for Au and **2** for Ag.

4. Cd/Hg @ Au₈

Since Cd and Hg are donors of valence electrons with $\nu = +2$, the clusters with $q = 0$ have a superatom electron count of $n = 10$. (Cd, Hg)@1⁰ has practically no H-L gap, and in fact, the D-like frontier orbitals have fractional occupation numbers. These isomers are higher in energy than (Cd, Hg)@2⁰, which have 1S²1P⁴_{y,z}1D²_z1P²_x configurations and exhibit small H-L gaps. The 1P_x and 1D²_z orbitals are shifted similarly as for (Au, Ag)@2⁺¹.

For $q = +2$, the clusters are eight-electron superatoms, with (Cd, Hg)@1⁺² having 1S²1P⁶ and (Cd, Hg)@2⁺² 1S²1P⁴_{y,z}1D²_z configurations. The filling order of the superatomic orbitals is the same as for the clusters with $q = 0$. Both isomers have large H-L gaps, with (Cd, Hg)@1⁺² having the largest of all the studied systems. However, (Cd, Hg)@2⁺² are lower in energy than the cubic isomers.

C. Magnetically induced current densities

To study the magnetically induced current density $\vec{j}^{(1)}(\vec{r})$ in all the systems, an external magnetic field $\vec{B} = (0, 0, 1\text{T})$ was imposed in the z -direction (Fig. 1) for all the clusters. To visualize the currents in different sectional planes of the clusters, the current densities were projected on three x - y planes at $z = 0.0 \text{ \AA}$, $z = 0.75 \text{ \AA}$, and $z = 2.22 \text{ \AA}$, starting from the z -coordinate of the central atom. Additionally, the paratropic, diatropic, and total contributions to these projected current densities were circularly integrated at different radii r from the center of the plane $(0, 0, z)$, showing which contribution dominates

at each radius. The projected current density fields and the circularly integrated currents for all the systems are shown in Figs. S5–S7.

To quantify the total current contributions over each of the three selected planes, radial integrals of the circularly integrated currents were calculated. These contributions are summarized in Tables S6–S8. We want to focus on those systems that showed the lowest energy, as summarized in Table I.

For (Rh, Ir)@2⁺¹, the major diatropic contribution is localized in the $z = 0.0 \text{ \AA}$ plane (Fig. S5) with the total radial integral contributions of -2.79 and $-2.22 \text{ \AA}^2 \text{ nA/T}$ (Table S6), respectively. Then, in these butterfly-like systems, the central atom is behaving as a single atom exhibiting a strong localized ring current within $\sim 1.0 \text{ \AA}$ from the nucleus. The $z = 2.22 \text{ \AA}$ plane shows also a localized diatropic contribution near the positions of the Au atoms (Fig. S5) that is accompanied by a paratropic contribution within $r = 1.0 \sim 2.0 \text{ \AA}$ from the center of the plane. In both systems, a global induced current is not observed.

A similar behavior is observed for the (Cd, Hg)@2^{0,+2} systems where a strong localized ring current is present near the central atom, higher for the neutral systems than for the charged ones (Fig. S7), with a total radial integral contribution of -1.71 and $-2.34 \text{ \AA}^2 \text{ nA/T}$ for Cd and Hg, respectively (see Table S8).

Finally, for the three other systems that showed a minimum in the butterfly-like structure, (Pd, Pt)@2⁺² and Ag@2⁺¹, a localized diatropic contribution is again observed around the central doping atom (Figs. S6 and S5) with total radial integral contributions of -1.94 and $-1.93 \text{ \AA}^2 \text{ nA/T}$ for the Pd and Pt clusters, respectively (Table S7), and $-1.48 \text{ \AA}^2 \text{ nA/T}$ for the Ag cluster (Table S6).

The only systems having the cubic structure lower in energy than the butterfly-like one are Pd@1⁰, Pt@1⁰, and Au@1⁺¹, which

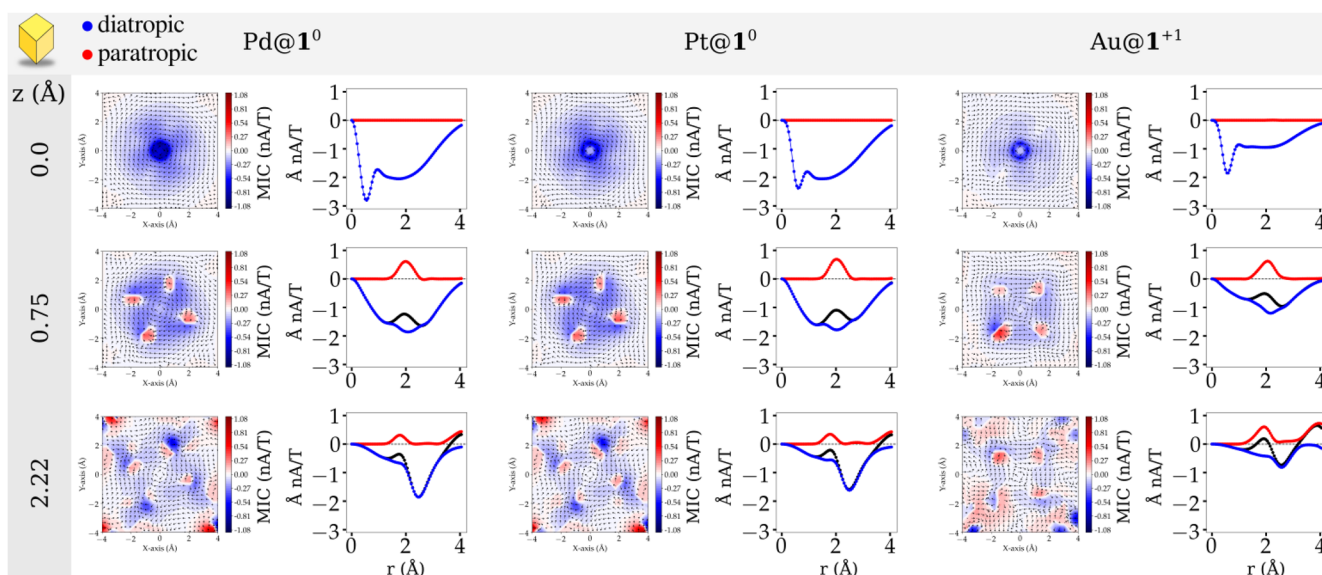


FIG. 4. Vectorial field of the magnetically induced current density and the circularly integrated current density for the cubic eight-electron superatoms Pd@1⁰, Pt@1⁰, and Au@1⁺¹ at the z -coordinate (Å). Diatropic (blue) and paratropic (red) contributions are shown. The total integrated current is shown in black. The external magnetic field \mathbf{B} is pointing toward the reader.

TABLE II. Total radial integrals of the circularly integrated current strength (Figs. S5–S7; in $\text{\AA}^2 \text{ nA/T}$) at radius $r = 4.0 \text{ \AA}$ from the center of an x - y plane located at $(0, 0, 0)$ in clusters $M@(\mathbf{1})^{0,+1,+2}$.

Rh@ $\mathbf{1}^{+1}$	Ir@ $\mathbf{1}^{+1}$	Ag@ $\mathbf{1}^{+1}$	Au@ $\mathbf{1}^{+1}$
−5.47	−4.96	−5.18	−3.09
Pd@ $\mathbf{1}^0$	Pd@ $\mathbf{1}^{+2}$	Pt@ $\mathbf{1}^0$	Pt@ $\mathbf{1}^{+2}$
−6.05	−4.56	−5.59	−4.2
Cd@ $\mathbf{1}^0$	Cd@ $\mathbf{1}^{+2}$	Hg@ $\mathbf{1}^0$	Hg@ $\mathbf{1}^{+2}$
−6.48	−3.64	−7.66	−3.81

are all eight-electron superatoms with large H–L gaps. The current density and circularly induced currents for these clusters can be seen in Fig. 4, showing that all the cubic structures support a diatropic current in the metal core. The total radially integrated contribution is the most diatropic one in the $z = 0.0 \text{ \AA}$ plane, with -6.05 , -5.59 , and $-3.09 \text{ \AA}^2 \text{ nA/T}$ for the Pd, Pt, and Au clusters, respectively. In fact, on this plane, there are no paratropic contributions in any of these clusters.

Comparing the cubic (1) and butterfly (2) structures in Figs. S5–S7, we can see that while both support diatropic currents at the $z = 0$ plane, this contribution is localized only around the central atom in butterfly structures. However, the cubic isomers have a substantial diatropic current over the whole metal core, as shown in Table II. Tables S5–S7 show that the total radially integrated current contributions of the cubic clusters are consistently more diatropic than in their butterfly-like counterparts. In both structures, the total integrated diatropic current also increases with the superatom electron count. This seems natural since a larger delocalized electron count can create a stronger response current in the same volume. Interestingly, the radial integrals for cubic structures show also diatropic contributions on the other planes, indicating a global induced current that is not diatropic only at the center but extends to the whole metallic core. This indicates that structures 1 are aromatic. The superatom electron count is shown in Table II

Figure 4 shows the effect of Pd and Pt doping for the induced currents compared to the cubic all-Au cluster. Both the maximum circularly integrated diatropic current and the total radially integrated diatropic contribution are bigger for the Pd and Pt doped clusters than for the all-Au cluster (for instance, in the plane of the dopant, the total diatropic contributions are as follows: Pd: -6.05 , Pt: -5.59 , and Au: $-3.09 \text{ \AA}^2 \text{ nA/T}$). This fact indicates that these dopants increase the aromaticity of the cluster. The order of aromaticity of these structures induced by the central atom follows the trend $\text{Pd} > \text{Pt} > \text{Au}$.

IV. CONCLUSIONS

In this work, we have studied the electronic structure and magnetically induced currents of doped $[M@Au_8L_8]^q$ superatoms ($M = \text{Pd, Pt, Ag, Au, Cd, Hg, Ir, and Rh}$; $L = \text{PPh}_3$; and $q = 0, +1, +2$) having 6–10 delocalized superatom electrons in the metal core. We

employed the gauge-including magnetically induced currents framework to compute the current susceptibility tensor and then the magnetically induced current density. This scheme has been previously used to give a quantitative measurement of the aromaticity/antiaromaticity in molecules via diatropic and paratropic contributions.⁴⁶ Analysis of all 24 different systems showed the following trends: (i) total integrated diatropic currents increase with the superatom electron count, (ii) the cubic-like clusters have generally larger diatropic currents than the butterfly-like clusters, and (iii) the total integrated diatropic currents, hence aromaticity, increases for eight-electron cubic clusters as $M = \text{Au} < \text{Pt} < \text{Pd}$, i.e., doping with zero-valent metals Pd and Pt increases the aromaticity. We hope that this work encourages further studies about the correlation between stability in closed shell superatoms and magnetic response properties, such as the magnetically induced current, helping to reach a better understanding about the aromatic character of complex 3D metal clusters and nanostructures.

SUPPLEMENTARY MATERIAL

See the supplementary material for total energies, HOMO–LUMO energy gaps, principal moments of inertia, PDOS, and MICs of all the systems studied in this work.

ACKNOWLEDGMENTS

This work was supported by the Academy of Finland (Grant Nos. 294217, 319208, and 315549) and through H.H. Academy Professorship. E.S. acknowledges the Finnish Cultural Foundation for a Ph.D. study grant. The computations were made at the Nanoscience Center of the University of Jyväskylä by utilizing the FCCI (Finnish Computing Competence Infrastructure, persistent identifier urn:nbn:fi:research-infras-2016072533) and at the Barcelona Supercomputing Center as a PRACE project (Grant No. 2018194723). B.Z.-G. acknowledges the funding from CONACyT (Project No. CB-2015-258647).

DATA AVAILABILITY

The data that support the findings of this study are available from the corresponding author upon reasonable request.

REFERENCES

- 1 A. M. Burkhardt, R. A. Loomis, C. N. Shingledecker, K. L. K. Lee, A. J. Remijan, M. C. McCarthy, and B. A. McGuire, “Ubiquitous aromatic carbon chemistry at the earliest stages of star formation,” *Nat. Astron.* **5**, 181 (2021).
- 2 P. v. R. Schleyer, “Introduction: Aromaticity,” *Chem. Rev.* **101**, 1115–1118 (2001).
- 3 A. Kekulé, “Sur la constitution des substances aromatiques,” *Bull. Mens. Soc. Chim. Paris* **3**, 98 (1865).
- 4 D. Chen, Y. Hua, and H. Xia, “Metallaaromatic chemistry: History and development,” *Chem. Rev.* **120**, 12994–13086 (2020).
- 5 J. Zhu, “Open questions on aromaticity in organometallics,” *Commun. Chem.* **3**, 161 (2020).

- ⁶A. Haags, A. Reichmann, Q. Fan, L. Egger, H. Kirschner, T. Naumann, S. Werner, T. Vollgraff, J. Sundermeyer, L. Eschmann, X. Yang, D. Brandstetter, F. C. Bocquet, G. Koller, A. Gottwald, M. Richter, M. G. Ramsey, M. Rohlfing, P. Puschnig, J. M. Gottfried, S. Soubatch, and F. S. Tautz, "Kekulene: On-surface synthesis, orbital structure, and aromatic stabilization," *ACS Nano* **14**, 15766–15775 (2020).
- ⁷J. A. N. F. Gomes and R. B. Mallion, "Aromaticity and ring currents," *Chem. Rev.* **101**, 1349–1384 (2001).
- ⁸A. Roglans, A. Pla-Quintana, and M. Solà, "Mechanistic studies of transition-metal-catalyzed [2 + 2 + 2] cycloaddition reactions," *Chem. Rev.* **121**, 1894–1979 (2021).
- ⁹J. Zhu, "Rational design of a carbon-boron frustrated Lewis pair for metal-free dinitrogen activation," *Chem. - Asian J.* **14**, 1413–1417 (2019).
- ¹⁰M. Solà, "Why aromaticity is a suspicious concept? Why?," *Front. Chem.* **5**, 22 (2017).
- ¹¹A. Hirsch, Z. Chen, and H. Jiao, "Spherical aromaticity in I_h symmetrical fullerenes: The $2(N + 1)^2$ rule," *Angew. Chem., Int. Ed.* **39**, 3915–3917 (2000).
- ¹²M. Solà, "Connecting and combining rules of aromaticity. Towards a unified theory of aromaticity," *Wiley Interdiscip. Rev.: Comput. Mol. Sci.* **9**, e1404 (2019).
- ¹³A. I. Boldyrev and L.-S. Wang, "All-metal aromaticity and antiaromaticity," *Chem. Rev.* **105**, 3716–3757 (2005).
- ¹⁴H. T. Pham and M. T. Nguyen, "Aromaticity of some metal clusters: A different view from magnetic ring current," *J. Phys. Chem. A* **122**, 1378–1391 (2018).
- ¹⁵A. I. Boldyrev and L.-S. Wang, "Beyond organic chemistry: Aromaticity in atomic clusters," *Phys. Chem. Chem. Phys.* **18**, 11589–11605 (2016).
- ¹⁶Z. Badri, S. Pathak, H. Fliegl, P. Rashidi-Ranjbar, R. Bast, R. Marek, C. Foroutan-Nejad, and K. Ruud, "All-metal aromaticity: Revisiting the ring current model among transition metal clusters," *J. Chem. Theory Comput.* **9**, 4789–4796 (2013).
- ¹⁷P. K. Chattaraj, *Aromaticity and Metal Clusters* (CRC Press, 2010).
- ¹⁸R. H. Mitchell, "Measuring aromaticity by NMR," *Chem. Rev.* **101**, 1301–1316 (2001).
- ¹⁹P. Cui, H.-S. Hu, B. Zhao, J. T. Miller, P. Cheng, and J. Li, "A multicentre-bonded $[Zn^I]_8$ cluster with cubic aromaticity," *Nat. Commun.* **6**, 6331 (2015).
- ²⁰H.-C. Hu, H.-S. Hu, B. Zhao, P. Cui, P. Cheng, and J. Li, "Metal-organic frameworks (MOFs) of a cubic metal cluster with multicentered Mn^I-Mn^I bonds," *Angew. Chem., Int. Ed.* **54**, 11681–11685 (2015).
- ²¹L. Geng, M. Weng, C.-Q. Xu, H. Zhang, C. Cui, H. Wu, X. Chen, M. Hu, H. Lin, Z.-D. Sun, X. Wang, H.-S. Hu, J. Li, J. Zheng, Z. Luo, F. Pan, and J. Yao, " $Co_{13}O_8$ —Metallooxubes: A new class of perovskite-like neutral clusters with cubic aromaticity," *Natl. Sci. Rev.* **8**, nwa201 (2020).
- ²²J.-C. Guo, L.-Y. Feng, C. Dong, and H.-J. Zhai, "A designer 32-electron superatomic CBe_8H_{12} cluster: Core-shell geometry, octacoordinate carbon, and cubic aromaticity," *New J. Chem.* **44**, 7286–7292 (2020).
- ²³N. Fedik, A. I. Boldyrev, and A. Muñoz-Castro, "Aromatic character of $[Au_{13}]^{5+}$ and $[MAu_{12}]^{4+/6+}$ ($M = Pd, Pt$) cores in ligand protected gold nanoclusters-interplay between spherical and planar σ -aromatics," *Phys. Chem. Chem. Phys.* **21**, 25215–25219 (2019).
- ²⁴A. Ghosh, O. F. Mohammed, and O. M. Bakr, "Atomic-level doping of metal clusters," *Acc. Chem. Res.* **51**, 3094–3103 (2018).
- ²⁵Q. Tang, G. Hu, V. Fung, and D.-e. Jiang, "Insights into interfaces, stability, electronic properties, and catalytic activities of atomically precise metal nanoclusters from first principles," *Acc. Chem. Res.* **51**, 2793–2802 (2018).
- ²⁶T. Higaki, Q. Li, M. Zhou, S. Zhao, Y. Li, S. Li, and R. Jin, "Toward the tailoring chemistry of metal nanoclusters for enhancing functionalities," *Acc. Chem. Res.* **51**, 2764–2773 (2018).
- ²⁷T. Tsukuda and H. Häkkinen, *Protected Metal Clusters: From Fundamentals to Applications* (Elsevier, 2015), Vol. 9.
- ²⁸S. Takano and T. Tsukuda, "Chemically modified gold/silver superatoms as artificial elements at nanoscale: Design principles and synthesis challenges," *J. Am. Chem. Soc.* **143**, 1683–1698 (2021).
- ²⁹F. Alkan, P. Pandeya, and C. M. Aikens, "Understanding the effect of doping on energetics and electronic structure for Au_{25} , Ag_{25} , and Au_{38} clusters," *J. Phys. Chem. C* **123**, 9516–9527 (2019).
- ³⁰K. A. Kacprzak, L. Lehtovaara, J. Akola, O. Lopez-Acevedo, and H. Häkkinen, "A density functional investigation of thiolate-protected bimetal $PdAu_{24}(SR)_{18}^z$ clusters: Doping the superatom complex," *Phys. Chem. Chem. Phys.* **11**, 7123–7129 (2009).
- ³¹D.-e. Jiang and S. Dai, "From superatomic $Au_{25}(SR)_{18}^-$ to superatomic $M@Au_{24}(SR)_{18}^q$ core-shell clusters," *Inorg. Chem.* **48**, 2720–2722 (2009).
- ³²W. Fei, S. Antonello, T. Dainese, A. Dolmella, M. Lahtinen, K. Rissanen, A. Venzo, and F. Maran, "Metal doping of $Au_{25}(SR)_{18}^-$ clusters: Insights and hindersights," *J. Am. Chem. Soc.* **141**, 16033–16045 (2019).
- ³³F. Alkan, A. Muñoz-Castro, and C. M. Aikens, "Relativistic DFT investigation of electronic structure effects arising from doping the Au_{25} nanocluster with transition metals," *Nanoscale* **9**, 15825–15834 (2017).
- ³⁴W. Choi, G. Hu, K. Kwak, M. Kim, D.-e. Jiang, J.-P. Choi, and D. Lee, "Effects of metal-doping on hydrogen evolution reaction catalyzed by MAu_{24} and M_2Au_{36} nanoclusters ($M = Pt, Pd$)," *ACS Appl. Mater. Interfaces* **10**, 44645–44653 (2018).
- ³⁵F. Wen, U. Englert, B. Gutrath, and U. Simon, "Crystal structure, electrochemical and optical properties of $[Au_9(PPh_3)_8](NO_3)_3$," *Eur. J. Inorg. Chem.* **2008**, 106–111.
- ³⁶K. P. Hall, B. R. C. Theobald, D. I. Gilmour, D. M. P. Mingos, and A. J. Welch, "Synthesis and structural characterization of $[Au_9\{P(p-C_6H_4OMe)_3\}_8](BF_4)_3$, a cluster with a centred crown of gold atoms," *J. Chem. Soc., Chem. Commun.* **1982**, 528–530.
- ³⁷S. Yamazoe, S. Matsuo, S. Muramatsu, S. Takano, K. Nitta, and T. Tsukuda, "Suppressing isomerization of phosphine-protected Au_9 cluster by bond stiffening induced by a single Pd atom substitution," *Inorg. Chem.* **56**, 8319–8325 (2017).
- ³⁸H. Shen, E. Selenius, P.-P. Ruan, X. Li, P. Yuan, O. Lopez-Estrada, S. Malola, S.-C. Lin, B. K. Teo, H. Häkkinen, and N. Zheng, "Solubility-driven isolation of a metastable nonagold nanocluster with body-centered cubic structure," *Chem. - Eur. J.* **26**, 8465 (2020).
- ³⁹L. N. Ito, B. J. Johnson, A. M. Muetting, and L. H. Pignolet, "Heterobimetallic gold-palladium phosphine cluster complexes. X-ray crystal and molecular structure of $[Au_8Pd(PPh_3)_8](NO_3)_2$," *Inorg. Chem.* **28**, 2026–2028 (1989).
- ⁴⁰J. J. Bour, R. P. F. Kanters, P. P. J. Schlebos, W. P. Bosman, H. Behm, P. T. Beurskens, and J. J. Steggerda, "Hetero-metallic clusters. Synthesis and characterization of $[PtAu_8(PPh_3)_8](NO_3)_2$ and $[HfPtAu_7(PPh_3)_8](NO_3)_2$," *Recl. Trav. Chim. Pays-Bas* **106**, 157–158 (1987).
- ⁴¹S. Takano, S. Ito, and T. Tsukuda, "Efficient and selective conversion of phosphine-protected $(MAu_8)^{2+}$ ($M = Pd, Pt$) superatoms to thiolate-protected $(MAu_{12})^{6+}$ or alkynyl-protected $(MAu_{12})^{4+}$ superatoms via hydride doping," *J. Am. Chem. Soc.* **141**, 15994–16002 (2019).
- ⁴²Y. Yuan, A. P. Kozlova, K. Asakura, H. Wan, K. Tsai, and Y. Iwasawa, "Supported Au catalysts prepared from Au phosphine complexes and as-precipitated metal hydroxides: Characterization and low-temperature CO oxidation," *J. Catal.* **170**, 191–199 (1997).
- ⁴³K. Hirata, R. Tomihara, K. Kim, K. Koyasu, and T. Tsukuda, "Characterization of chemically modified gold and silver clusters in gas phase," *Phys. Chem. Chem. Phys.* **21**, 17463–17474 (2019).
- ⁴⁴A. Cirri, H. M. Hernández, and C. J. Johnson, "Hydride, chloride, and bromide show similar electronic effects in the $Au_9(PPh_3)_8^{3+}$ nanocluster," *Chem. Commun.* **56**, 1283–1285 (2020).
- ⁴⁵P. Lazeretti, "Assessment of aromaticity via molecular response properties," *Phys. Chem. Chem. Phys.* **6**, 217–223 (2004).
- ⁴⁶O. López-Estrada, B. Zuniga-Gutierrez, E. Selenius, S. Malola, and H. Häkkinen, "Magnetically induced currents and aromaticity in ligand-stabilized Au and AuPt superatoms," *Nat. Commun.* **12**, 2477 (2021).
- ⁴⁷F. London, "Théorie quantique des courants interatomiques dans les combinaisons aromatiques," *J. Phys. Radium* **8**, 397 (1937).
- ⁴⁸B. Zuniga-Gutierrez, G. Geudtner, and A. M. Köster, "NMR shielding tensors from auxiliary density functional theory," *J. Chem. Phys.* **134**, 124108 (2011).
- ⁴⁹H. Fliegl, D. Sundholm, S. Taubert, J. Jusélius, and W. Klopper, "Magnetically induced current densities in aromatic, antiaromatic, homoaromatic, and nonaromatic hydrocarbons," *J. Phys. Chem. A* **113**, 8668–8676 (2009).
- ⁵⁰P. Lazeretti, "Ring currents," *Prog. Nucl. Magn. Reson. Spectrosc.* **36**, 1–88 (2000).
- ⁵¹A. Soncini, P. W. Fowler, P. Lazeretti, and R. Zangari, "Ring-current signatures in shielding-density maps," *Chem. Phys. Lett.* **401**, 164–169 (2005).

- ⁵²B. Zuniga-Gutierrez, G. Geudtner, and A. M. Köster, "Magnetizability tensors from auxiliary density functional theory," *J. Chem. Phys.* **137**, 094113 (2012).
- ⁵³T. Helgaker, M. Jaszuński, and K. Ruud, "Ab initio methods for the calculation of NMR shielding and indirect spin-spin coupling constants," *Chem. Rev.* **99**, 293–352 (1999).
- ⁵⁴C. J. Jameson and A. D. Buckingham, "Nuclear magnetic shielding density," *J. Phys. Chem.* **83**, 3366–3371 (1979).
- ⁵⁵C. J. Jameson and A. D. Buckingham, "Molecular electronic property density functions: The nuclear magnetic shielding density," *J. Chem. Phys.* **73**, 5684–5692 (1980).
- ⁵⁶W. Bieger, G. Seifert, H. Eschrig, and G. Grossmann, "LCAO $X\alpha$ calculations of nuclear magnetic shielding in molecules," *Chem. Phys. Lett.* **115**, 275–280 (1985).
- ⁵⁷M. Karplus and H. J. Kolker, "Magnetic interactions in lithium hydride," *J. Chem. Phys.* **35**, 2235–2236 (1961).
- ⁵⁸R. M. Stevens, R. M. Pitzer, and W. N. Lipscomb, "Perturbed Hartree-Fock calculations. I. Magnetic susceptibility and shielding in the LiH molecule," *J. Chem. Phys.* **38**, 550–560 (1963).
- ⁵⁹H. Sambe, "Properties of induced electron current density of a molecule under a static uniform magnetic field," *J. Chem. Phys.* **59**, 555 (1973).
- ⁶⁰G. P. Arrighini, M. Maestro, and R. Moccia, "Magnetic properties of polyatomic molecules. II. Proton magnetic shielding constants in H_2O , NH_3 , CH_4 , and CH_3F ," *J. Chem. Phys.* **52**, 6411–6415 (1970).
- ⁶¹P. Lazzeretti, M. Malagoli, and R. Zanasi, "Computational approach to molecular magnetic properties by continuous transformation of the origin of the current density," *Chem. Phys. Lett.* **220**, 299–304 (1994).
- ⁶²P. Lazzeretti, "Current density tensors," *J. Chem. Phys.* **148**, 134109 (2018).
- ⁶³A. Koster, G. Geudtner, A. Alvarez-Ibarra, P. Calaminici, M. Casida, J. Carmona-Espindola, V. Dominguez, R. Flores-Moreno, G. Gamboa, A. Goursot, T. Heine, A. Ipatov, A. de la Lande, F. Janetzko, J. del Campo, D. Mejia-Rodriguez, J. U. Reveles, J. Vasquez-Perez, A. Vela, B. Zuniga-Gutierrez, and D. Salahub, deMon2k, version 6, the deMon developers, Cinvestav, Mexico City, 2018, <http://www.demon-software.com/>.
- ⁶⁴J. J. Mortensen, L. B. Hansen, and K. W. Jacobsen, "Real-space grid implementation of the projector augmented wave method," *Phys. Rev. B* **71**, 035109 (2005).
- ⁶⁵J. Enkovaara, C. Rostgaard, J. J. Mortensen, J. Chen, M. Dulak, L. Ferrighi, J. Gavnholt, C. Glinsvad, V. Haikola, H. A. Hansen, H. H. Kristoffersen, M. Kuisma, A. H. Larsen, L. Lehtovaara, M. Ljungberg, O. Lopez-Acevedo, P. G. Moses, J. Ojanen, T. Olsen, V. Petzold, N. A. Romero, J. Stausholm-Møller, M. Strange, G. A. Tritsarlis, M. Vanin, M. Walter, B. Hammer, H. Häkkinen, G. K. H. Madsen, R. M. Nieminen, J. K. Nørskov, M. Puska, T. T. Rantala, J. Schiøtz, K. S. Thygesen, and K. W. Jacobsen, "Electronic structure calculations with GPAW: A real-space implementation of the projector augmented-wave method," *J. Phys.: Condens. Matter* **22**, 253202 (2010).
- ⁶⁶J. P. Perdew, K. Burke, and M. Ernzerhof, "Generalized gradient approximation made simple," *Phys. Rev. Lett.* **77**, 3865–3868 (1996).
- ⁶⁷M. Walter, J. Akola, O. Lopez-Acevedo, P. D. Jadzinsky, G. Calero, C. J. Ackerson, R. L. Whetten, H. Grönbeck, and H. Häkkinen, "A unified view of ligand-protected gold clusters as superatom complexes," *Proc. Natl. Acad. Sci. U. S. A.* **105**, 9157–9162 (2008).
- ⁶⁸B. P. Pritchard, D. Altarawy, B. Didier, T. D. Gibson, and T. L. Windus, "New basis set exchange: An open, up-to-date resource for the molecular sciences community," *J. Chem. Inf. Model.* **59**, 4814–4820 (2019).
- ⁶⁹P. Calaminici, F. Janetzko, A. M. Köster, R. Mejia-Olvera, and B. Zuniga-Gutierrez, "Density functional theory optimized basis sets for gradient corrected functionals: $3d$ transition metal systems," *J. Chem. Phys.* **126**, 044108 (2007).